New characterization measures of pore shape and connectivity applied to coatings used for controlled drug release

Citation for the original published paper (version of record):
Eriksson Barman, S., Fager, C., Röding, M. et al (2021). New characterization measures of pore shape and connectivity applied to coatings used for
controlled drug release. Journal of Pharmaceutical Sciences, 110(7): 2753-2764.
http://dx.doi.org/10.1016/j.xphs.2021.02.024

Journal of Pharmaceutical Sciences 000 (2021) 1−12

Contents lists available at ScienceDirect

Journal of Pharmaceutical Sciences

journal homepage: www.jpharmsci.org

Pharmaceutics, Drug Delivery and Pharmaceutical Technology

New characterization measures of pore shape and connectivity applied to coatings used for controlled drug release

Sandra Barman[a,*], Cecilia Fager[b], Magnus Röding[a,c], Niklas Lorén[b,c],
Christian von Corswant[d], Eva Olsson[b], David Bolin[e], Holger Rootzén[a]

[a] *Department of Mathematical Sciences, Chalmers University of Technology and the University of Gothenburg, 412 96 Gothenburg, Sweden*
[b] *Department of Physics, Chalmers University of Technology, 412 96 Gothenburg, Sweden*
[c] *Agriculture and Food, RISE Research Institutes of Sweden, Gothenburg, Sweden*
[d] *Oral Product Development, Pharmaceutical Technology & Development, Operations, AstraZeneca, Gothenburg, Sweden*
[e] *CEMSE Division, King Abdullah University of Science and Technology, Thuwal, Saudi Arabia*

ARTICLE INFO

Article history:
Received 9 November 2020
Revised 26 January 2021
Accepted 16 February 2021
Available online xxx

ABSTRACT

Pore geometry characterization-methods are important tools for understanding how pore structure influences properties such as transport through a porous material. Bottlenecks can have a large influence on transport and related properties. However, existing methods only catch certain types of bottleneck effects caused by variations in pore size. We here introduce a new measure, geodesic channel strength, which captures a different type of bottleneck effect caused by many paths coinciding in the same pore. We further develop new variants of pore size measures and propose a new way of visualizing 3-D characterization results using layered images. The new measures together with existing measures were used to characterize and visualize properties of 3-D FIB-SEM images of three leached ethyl-cellulose/hydroxypropyl-cellulose films. All films were shown to be anisotropic, and the strongest anisotropy was found in the film with lowest porosity. This film had very tortuous paths and strong geodesic channel-bottlenecks, while the paths through the other two films were relatively straight with well-connected pore networks. The geodesic channel strength was shown to give important new visual and quantitative insights about connectivity, and the new pore size measures provided useful information about anisotropies and inhomogeneities in the pore structures. The methods have been implemented in the freely available software MIST.

Introduction

The pore geometry to a large extent determines the rate of diffusive transport through a porous material. Structural properties that can have a large impact on the diffusive transport rates are pore volume fraction; pore sizes and shapes; lengths of paths through the pore system; dead-ends; and bottleneck effects[1,2] (because the governing equations are mathematically equivalent, this also holds for electrical and thermal conductivity[3]). Information about connectivity properties such as path lengths and bottleneck effects can only be obtained from 3-D representations of the material. Advances in microscopy techniques have made it possible to obtain detailed images of the 3-D geometry of porous materials.[4−6] To make full use of these images, characterization methods that capture the important properties of the pore geometry are needed. Nevertheless, despite the availability of both 3-D images and characterization methods, often only simple measures such as the total porosity,[7] the spherical pore size distribution, or the chord-length distribution[8] are reported. In particular, these measures do not give any information about anisotropy or about connectivity of pore structures.

Existing pore geometry measures include pore sizes computed using different structuring elements, such as spheres, ellipsoid, and lines, and local porosity. Path lengths through the pore network are characterized by the geodesic tortuosity and measures the length of geodesic paths.[9] A geodesic path is here the shortest path which lies completely within the pore space and which connects the top to the bottom and goes through a specified point. Geodesic paths and tortuosities are powerful methods that can be used to visually explore how the pore network is connected and geodesic tortuosity is often a good predictor of diffusive transport.[10,11] It is well known that bottleneck effects caused by pore size variation, i.e. constrictivity effects, can have a large effect on transport through porous materials, see e.g. Petersen,[1] Van Brakel and Heertjes,[12] Dullien[13](p. 228) and Siepmann

---

[*] Corresponding author.
E-mail address: sandrabarman@gmail.com (S. Barman).

https://doi.org/10.1016/j.xphs.2021.02.024

et al.[2(ch.9)] Measures of this type of constrictivity effect have been introduced in recent years in Berg[14] and Holzer et al.[15] In Holzer et al.,[15] the constrictivity is computed using pore sizes with respect to structuring elements and from mercury intrusion porosimetry (MIP)-pore sizes that are designed to match a physical experiment. This constrictivity measure together with the tortuosity has been shown to be a good predictor of diffusive transport.[10] Still, existing constrictivity measures do not capture all aspects of bottleneck effects.

This paper introduces a new geometric measure, geodesic channel strength, which quantifies an important property of the network connecting the pores, viz. parts of the pore structure where many geodesic paths coincide. The measure provides a method to simplify the network which can be used to visually identify and to quantify important structural features such as bottlenecks in the data and for prediction of diffusive transport. The geodesic channel strength measures a type of bottleneck effect that is different from the already existing constrictivity measures.

The paper also proposes new measures of the local shape of pores obtained as maxima, taken in different directions, of pore sizes with respect to circles and lines. These maxima gave additional shape information, which was summarized as elongation and ellipsoid factors. To the best of our knowledge such maxima and shape factors have not been considered in earlier literature. We further introduce a new way of visualizing results in 3-D by layering images with different opacities.

Leached ethyl-cellulose (EC)/hydroxypropyl-cellulose (HPC) films are used as coating for controlled drug release from pharmaceutical pellets. The drug diffuses through the pore structure that forms when the HPC is leached out, and the pore geometry controls how fast the drug is released. Previous work detailing the 3-D microstructure of this type of EC/HPC polymers can be found in Marucci et al.[16,17] and in Andersson et al.,[18] where the material has been imaged using confocal microscopy and scanning electron microscopy. Transport through these coatings has been visualized using in situ environmental scanning electron microscopy in Jansson et al.[19] The same type of polymer has also been characterized with respect to pore shape and branching points in Häbel et al.,[20,21] and a visualization of the interconnectivity of the three films which are used in this work can be found in Fager et al.[22]

In the present paper, we used our new measures, together with local porosity, pore size with respect to spheres, circles and lines, constrictivity measures, and measures based on distances through the pore structure, to extract important features of the pore geometry of 3-D images of EC/HPC films. The images were obtained from combined focused ion beam and scanning electron microscopy (FIB-SEM) tomography of films where the aqueous soluble HPC phase had been leached, leaving the EC porous network intact.[23] The advantage of using scanning electron microscopy in contrast to, e.g., confocal microscopy is the high spatial resolution, and the focused ion beam tomography in combination with the scanning electron microscope enables a 3-D reconstruction of the porous microstructure. Other sequential imaging techniques that can be used for 3-D reconstruction of porous materials, apart from confocal microscopy[24] and electron microscopy,[25] are X-ray tomography[26] and neutron tomography.[27]

In the next section the processes used to manufacture the EC/HPC films, to leach the HPC phase, to record experimental 3-D data and to binarize the images are outlined. The following section describes the pore structure characterization methods. The results are then given, followed by a discussion of the main conclusions. Details about the construction of the layered images, two videos illustrating the advantages with using layered images, and the method used to compute the geodesic paths can be found in the electronic supplementary material.

Materials and methods

Data acquisition

Ethyl cellulose/hydroxypropyl cellulose polymer films

The polymer films were produced from the water soluble polymer, HPC, and the water insoluble polymer, EC. The two polymers were dissolved in ethanol and sprayed onto a rotating drum to create a film. The spraying direction was the direction of transport through the film, corresponding to the direction of transport through the coatings of pharmaceutical pellets. After drying, the films were cut off from the drum and the HPC were leached out to create 0.5 cm × 0.5 cm square porous films. The weight percentages of the water soluble polymer HPC were 22, 30, and 45. The films were denoted HPC22, HPC30 and HPC45, respectively. For a detailed description of the production process see Fager et al.[22]

Focused ion beam scanning electron microscopy and 3-D image segmentation

A FIB beam was used to sequentially prepare cross sections of the EC/HPC films and a SEM was used to image the cross sections. This produced stacks of 200 2-D images per film. Fig. 1 shows one of the 2-D images from each stack. Again, see Fager et al.[22] for a detailed description. Segmentation of the image data into solid and pore was performed in the following fashion: For each data set, manual segmentation was performed in 100 randomly selected 2-D regions of size 256 × 256 pixels. So-called linear scale-space features, i.e., a set of Gaussian smoothed images at different scales were extracted (using Gaussian filters with standard deviations sigma = 1, 2, 4, 8, 16, 32, 64, and 128 pixels) for the slice to be segmented and five adjacent slices in each direction. These features were used to train a random forest classifier (combining the output of 101 decision tree classifiers) which is then applied to the full data sets. The resulting segmented images (Fig. 2) were used to describe the porous network. For more details on the image segmentation, the reader is referred to Röding et al.,[28] in which an almost identical segmentation work flow was used.

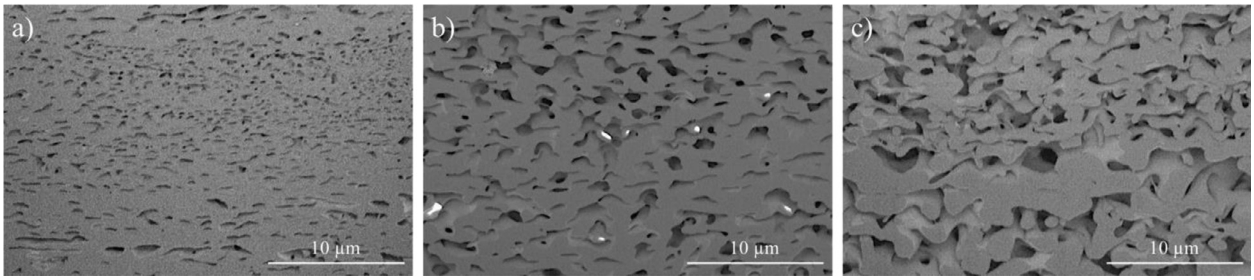

Fig. 1. Cross sectional surfaces, imaged using a FIB-SEM backscattered electron detector, of (a) HPC22, (b) HPC30 and (c) HPC45.

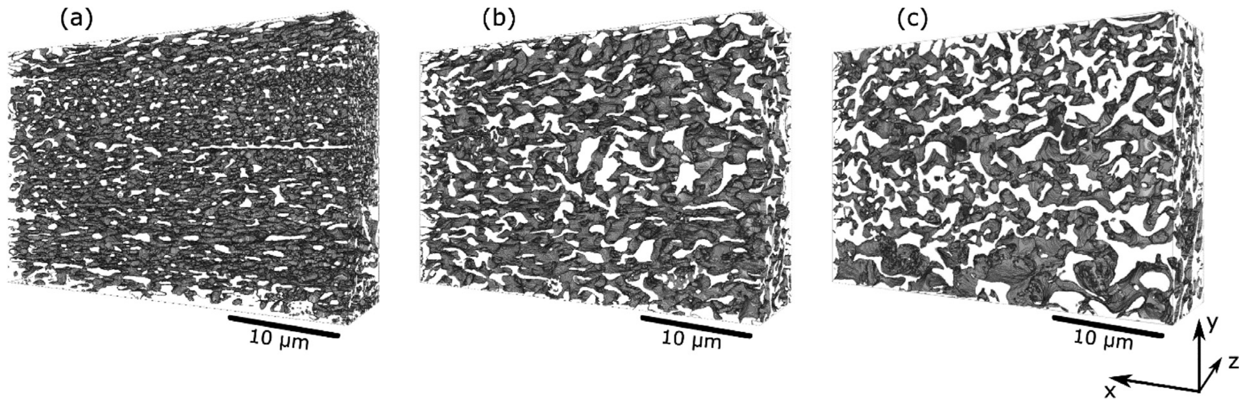

Fig. 2. Binarized pore structures of (a) HPC22, (b) HPC30 and (c) HPC45. Pores are shown in white. The slices were milled away in the *z*-direction, and *y* is the direction of diffusive transport.

To avoid edge effects the images were cropped close to the boundary, removing 11% of the voxels in the *x*-direction. The images were also sub-sampled, taking every fifth voxel in the *x*- and *y*-direction, so that the voxel size was 50 nm in all directions. This was necessary since equal voxel size in all directions is a requirement of the built-in Matlab function bwdistgeodesic[29] which was used to compute geodesic paths, geodesic tortuosity and geodesic channel strength. The resulting images were of size 500 × 750 × 200 voxels.

A slice from each of the three films is shown in Fig. 1 and the binarized pore structures that the characterization methods were applied to are displayed in Fig. 2.

Characterization methods

New method: geodesic channel strength

The geodesic channel strength as defined below quantifies how pores are interconnected. A channel of high strength by this definition is a part of the pore structure where many geodesic paths coincide. The channel measure enables the visualization and quantification of main channels, i.e. points with relatively high channel strength. This measure highlights an important property of the network connecting the pores; visualizing only main channels can simplify an otherwise complex network, making it easier to detect important structural features. In some cases when there are channels of varying strength and some channels have a particularly high strength it can be concluded that there is a bottleneck effect. However, it is important to also take pore size and alternative pathways into account before drawing this conclusion. A channel of high strength might not be a bottleneck if it has a large pore size relative to the pores leading into the channel. Alternative pathways close to the high strength channel could also reduce the bottleneck effect.

A geodesic path, denoted $GeoPath(p)$, as described in the introduction, is a path that (1) lies completely within the pore space, (2) is the shortest path that connects the top of the pore structure to the bottom of the pore structure in the chosen direction (x, y or z),[1] and (3) passes through the point p. Computation of shortest paths with restrictions on the space that can be travelled can be found in robotics, visual computing, and image analysis,[30,31,32,33] and has been used in the context of material science in Lindquist et al.[34] and in Peyrega and Jeulin[9] to visualize paths through a material. The left panel of Fig. 3 illustrates the concept of a geodesic path in a 2-D pore structure. This 2-D network was extracted from a 930 × 6 × 750 subset of the original binarized HPC45 sample by projection of the six slices in the y-direction to one slice.

The algorithm used to compute the geodesic channel strength in the three EC/HPC films was implemented as follows: First, a set S consisting of around 9000 points p were distributed evenly throughout the pore structure. The distribution was done by dividing the pore structure into small sections, and randomly placing points p uniformly in each section. The number of points placed in each small section, out of the total 9000 points, was proportional to the pore volume of the small section. The corresponding geodesic path $GeoPath(p)$ (computed in the chosen direction) was then computed for every distributed point p. Each path was set to have a thickness of 20 voxels (corresponding to 1 μm) to make the channel measure easier to visualize.

This resulted in a set of paths $G = \{GeoPath(p)\colon p \in S\}$. Finally, the geodesic channel strength, denoted $GeoChannel(p')$, is defined as the percentage of paths in G that passed through the point p'. $GeoChannel(p')$ was computed for all points p' in the pore structure. See the electronic supplementary material for a description of the algorithm for computing the geodesic paths.

An example of the geodesic channel measure is shown in the right panel of Fig. 3. It clearly shows a significant aspect of the 2-D network connecting the top and bottom: there are four main channels from the middle to the top, whereas there are only three main channels from the middle to the bottom. Note also that the three geodesic paths $GeoPath(p)$ in the left panel follow to a large extent the main geodesic channels, except when the paths are close to their respective points p.

Geodesic tortuosity

The point-wise geodesic tortuosity is defined as

$$\tau_{\mathrm{dir}}(p) = l(GeoPath(p))/L,$$

where $l(GeoPath(p))$ is the length of the geodesic path corresponding to p, computed in direction dir, and L is the thickness of the pore structure in this direction. The tortuosity thus measures the length of the geodesic path relative to the length of the pore structure in the direction the path is computed. A 2-D example of the tortuosity is shown in Fig. 4, where the color of each point corresponds to the point-wise tortuosity-value in that point. It is clear from the tortuosity that geodesic paths on the left are longer than paths on the right (compare with the three paths shown in Fig. 3).

Our definition computes the tortuosities for the full pore structure, as is done in Peyrega and Jeulin[9] and Barman et al.,[11] instead of using the common method where tortuosities are only computed for geodesic paths at the top layer of the pore structure (i.e., tortuosities are only computed corresponding to geodesic paths $GeoPath(p)$ for points p in the top layer).[10,34] In Barman et al.,[11] computing tortuosities for the full pore structure was found to give better diffusive transport prediction.

---

[1] Note that the top and bottom of the pore structure refers to the top and bottom in the chosen direction.

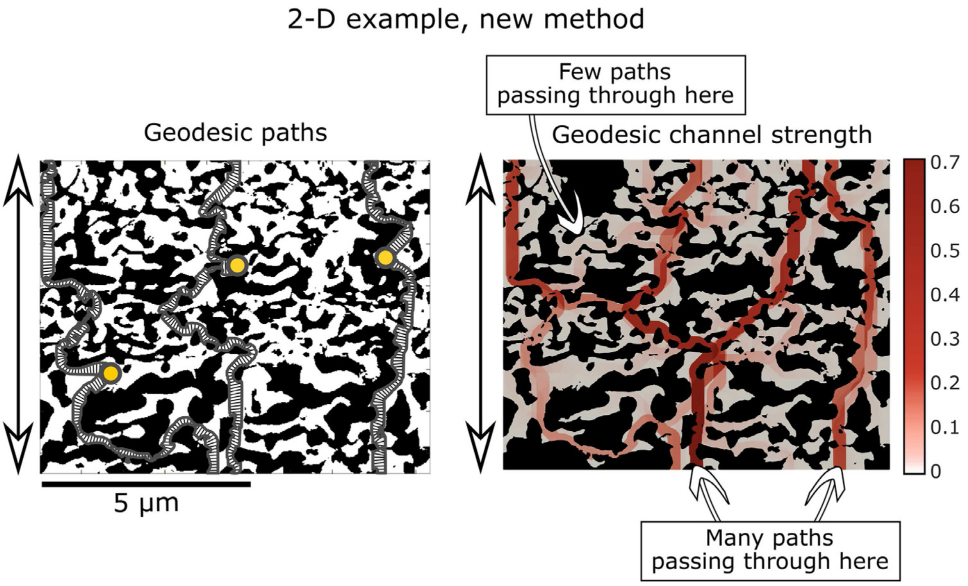

Fig. 3. Example illustrating the connection between geodesic paths and geodesic channel strength on a 2-D pore structure extracted from HPC45. Left: Three geodesic paths *GeoPath (p)*. The points *p*, for which *GeoPath*(*p*) is the shortest path connecting *p* to the top and the bottom, are marked with yellow circles. The matrix is shown in black. Right: The geodesic channel strength computed from 3000 geodesic paths connecting the top and bottom. The channel strength is only shown for pores that are connected to the top and bottom. The matrix and pores that are not connected are shown in black. Double-headed arrows indicate the direction of the geodesic paths and channel strength. (For interpretation of the references to color in this figure legend, the reader is referred to the web version of this article.)

Local porosity

The local porosity was computed similarly to what was done in Hilfer,[35] by computing the porosity for subsets of the pore structure: The pore structure was first divided into 45 × 30 × 3 boxes, i.e. the *x*-direction was divided into 45 parts of roughly equal size, the *y*-direction into 30 parts of roughly equal size, and the *z*-direction into 3 parts of roughly equal size. The porosity was then computed for each combination of 3 × 3 × 3 neighboring boxes, resulting in local porosity values on a 43 × 28 × 1 grid.

Local pore sizes

Local pore sizes are computed relative to simple geometrical objects, which are called structuring elements. The pore size in a point *p* is defined as the size of the largest rescaled structuring

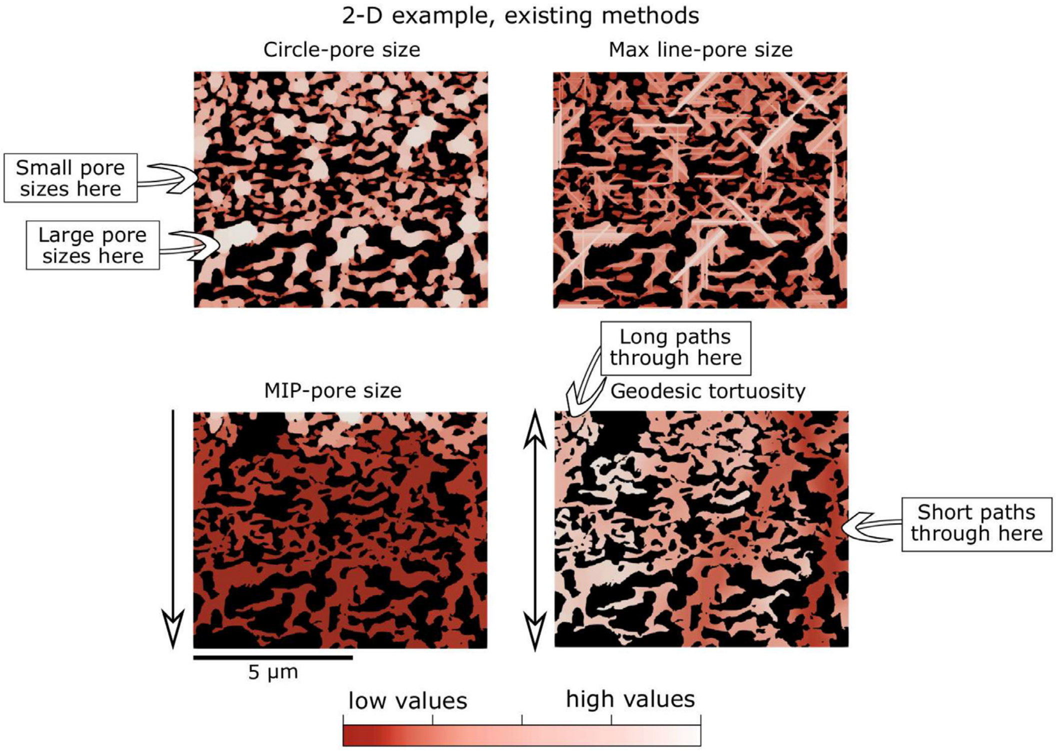

Fig. 4. Examples, using the same pore structure as in Fig. 3, showing circle-pore sizes, maximal line-pore sizes, MIP-pore sizes computed from the top and geodesic tortuosities corresponding to paths connecting the top and bottom. Arrows indicate the direction the connectivity measures were computed in. MIP-pore sizes were only computed for pores that are connected to the top, and tortuosity values were only computed for pores that are connected to the top and bottom.

Table 1
Pore shape measures and the two pore shape factors. The mean, minimum, maximum and standard deviation of the sphere-pore size ps_{sphere}, maximal circle-pore size $ps_{circ,\max}$, and maximal line-pore size $ps_{line,\max}$ are given in μm.

	HPC22	HPC30	HPC45
ps_{sphere}, mean (min, max) [st.dev.]	0.35 (0.05, 0.95) [0.14]	0.60 (0.05, 1.55) [0.26]	0.72 (0.05, 2.15) [0.36]
$ps_{circ,\max}$, mean (min, max) [st.dev.]	0.62 (0.05, 2.95) [0.35]	1.00 (0.05, 2.55) [0.39]	1.18 (0.05, 3.15) [0.52]
ellipsoid factor	2.0	1.9	2.0
$ps_{line,\max}$, mean (min, max) [st.dev.]	1.42 (0.05, 11.95) [0.99]	2.57 (0.05, 8.55) [0.94]	3.39 (0.05, 11.75) [1.32]
elongation factor	4.7	5.3	6.3

element that can fit within the pore space and cover p. Each point in the pore space is in this way given a local size. These local pore sizes provide an intuitive measure of size for pore geometries for which there are no well-defined pore shapes. Local pore sizes, or granulometries as they are also called, were introduced in Matheron[36] and is a common tool in image analysis.[33] Different structuring elements quantify different properties of the pore geometry. For the 3-D data we used spheres, circles and line segments as structuring elements. The sphere-sizes give non-directional size information, whereas circles and line-sizes give information about pore shape and anisotropy. The notation for the structuring elements is B_{sphere} for a sphere structuring element, $B_{\text{circ,plane}}$ for a circle located in the plane, where the plane is either of the sub-planes (x, y), (x, z), or (y, z), and $B_{\text{line,dir}}$ for a line segment structuring element in direction dir, with dir being the direction of the x-, y-, or z-axis, a diagonal direction in the (x, y)-, (x, z)- and (y, z)-planes, or a diagonal direction in the unit cube. Thus three circle-sizes and 13 line-sizes are computed. The local pore size is denoted ps^* for structuring element B^*.

We also define two new local pore size measures: the local maximal circle-pore size $ps_{\text{circ,max}}$, which is obtained by taking the maximum of $ps_{\text{circ,plane}}$ over all three planes, and the local maximal line-pore size $ps_{\text{line,max}}$, which is obtained by taking the maximum of $ps_{\text{line,dir}}$ over all thirteen directions. These maximal pore sizes are used to define an elongation factor and an ellipsoid factor that summarize the shape of the pores. The factors are defined by comparing the maximal circle size and the maximal line size respectively to the sphere size, and taking the mean over all points in the pore space, as $Elong = \text{mean}(ps_{\text{line,max}}/ps_{\text{sphere}})$ and $Ellips = \text{mean}(ps_{\text{circ,max}}/ps_{\text{sphere}})$. 2-D illustrations of circle-pore sizes and maximal line sizes are shown in the top of Fig. 4.

MIP-pore sizes

The MIP-pore size in a point p, denoted $ps_{\text{MIP,dir}}$, is the size of the largest sphere that can travel through the pore space from the top of the pore structure in the chosen direction to the point p, and that can cover p. The MIP-pore size measure is illustrated in Fig. 4.

The ratio between the median MIP-bottleneck size, median(ps_{MIP}), and the median of the sphere-pore size, median(ps_{sphere}), is termed the constrictivity. The MIP-pore size and the constrictivity has previously been proven useful as measures of interconnectivity and bottleneck effects.[10,37,38]

Computation

The spheres, circles, and diagonal line-segment structuring elements that were used to compute the local pore sizes are approximations of the ideal shape on the finite grid of the microscopy image.[33] This approximation is better for larger structuring elements. For computational efficiency, not all possible local pore sizes were computed. For the algorithm to compute the local MIP-bottleneck size, see Münch and Holzer.[39]

The characterization methods were implemented in Matlab.[29] The geodesic tortuosity, geodesic paths and geodesic channel strengths were computed from the geodesic distance transform obtained from the Matlab function bwdistgeodesic. The algorithm that was implemented for computing the geodesic paths is given in the electronic supplementary information. The geodesic tortuosity was obtained directly from the geodesic distance transform, and the geodesic channel strength was computed from a collection of geodesic paths as described above. The 3-D visualizations of characterization results were created using Paraview.[40] The image layering (see the electronic supplementary material) can be done in most image editing software, here it was done using Inkscape.[41] The videos in the electronic supplementary material were created using Paraview and VideoPad Professional.[42]

All characterization methods have been implemented in the freely available software MIST,[43] which soon will be available to download from here.[2]

Results

The porosity for the three EC/HPC films was calculated to 18% for HPC22, 29% for HPC30 and 42% for HPC45. The measured pore volume fractions in the cropped images that were used for the characterization, which had voxels close to the x-direction removed because of edge effects from the binarization, were relatively close to those of the original binarized images, with 18% for HPC22, 30% for HPC30 and 41% for HPC45.

The characterization results are inevitably biased because of boundary effects. The sample size is much smaller in the z-direction, which should result in stronger boundary effects in the z-direction. However, since the sample sizes in the x- and y-direction are similar, the results for these directions are comparable and hence some of the results are given only for the x- and y-directions. Additionally, the most interesting results are for the y-direction, the direction corresponding to drug transport, and some results are only presented for this direction.

Pore size and shape

Table 1 shows that the sphere-pore sizes, maximal circle-pore sizes and maximal line-pore sizes increase as the pore volume increases (with the exception of the max value of the maximal circle- and of the maximal line-pore size, which is high for HPC22 due to inhomogeneities, see the discussion below). The sphere-sizes are also smaller than the circle-sizes which in turn are smaller than the line-sizes, as can be expected. The same trends are observed in Fig. 5. The ellipsoid shape factor stays relatively constant, whereas the elongation shape factor increases as the pore volume increases (Table 1).

What stands out in Fig. 6 is that there is a big difference in how often the line size in the x-direction (numbered 1) is the largest compared to how often the line size in the y-direction (numbered 2) is largest. This line size trend is relatively strong in all films, but is stronger for lower pore volume fractions. The same trend with smaller sizes in the y-direction can be found for the diagonal lines in the planes (numbered 4-9) for HPC22, i.e., the diagonal lines are more frequently the largest in the xz-plane (numbered 8-9) compared to lines in the planes that include

---

[2] https://mist.math.chalmers.se

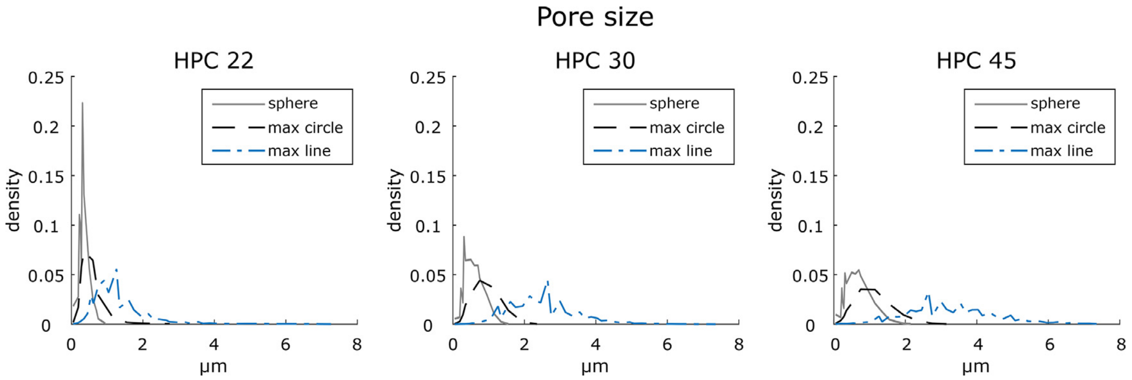

Fig. 5. Densities of sphere sizes, maximal circle sizes and maximal line sizes, for all three films.

the *y*-direction (numbered 4-7). The four cross-diagonal lines in the unit-cube (numbered 10-13) do not show large differences between the different directions.

The HPC22 film is seen in Panel (b) of Fig. 7 to have strongly inhomogeneous *xz*-circle sizes, i.e. $ps_{circ,xz}$ varies markedly between *y*-slices. This is, however, not the case for HPC30 and HPC45 in Panel (b), nor is it the case for the other two circle-pore sizes, $ps_{circ,yz}$ and $ps_{circ,xy}$ for any of the three films (Panels (a) and (c)). The largest value of the maximal circle-pore size $ps_{circ,\max}$ (and of the maximal line-pore size $ps_{line,\max}$) is also larger for HPC22 than for HPC30 (Table 1), which goes against the trend of pore sizes increasing with increasing porosity.

Connectivity

By Table 2 the proportion of connected pores is much lower in HPC22 than in HPC30 and HPC45. The MIP-pore size and the constrictivity show that bottleneck effects caused by variation in pore size are stronger in HPC22 than in the other two films. The median MIP-pore size of HPC22 corresponds to bottlenecks of one voxel, meaning that the largest sphere that can reach at least half of the film from the top is a sphere that consists of only one voxel.

The local porosities shown in Fig. 8 are averages of the porosity in boxes that span the whole film in the *z*-direction but that only occupy a small portion of the film in the *x*- and *y*-direction. The figure shows that there is quite high variation in all three films, and that there are layers in the *y*-direction with low porosity (see the layers marked with a dashed frame in the figure).

Visual inspection of geodesic paths

The geodesic paths computed in HPC22, shown in Fig. 9, seem more disordered than the paths through HPC30 and HPC45, which are more evenly distributed throughout the pore space and which are less winded. The layers in HPC22 with low porosities (marked with a dashed frame in yellow in Fig. 8) are marked with a yellow box. It looks as though the connectivity~~,~~ through this layer is poor, as the computed geodesic paths all pass through two parts of this box, see the yellow arrows.

Connectivity measured by geodesic tortuosity (path lengths)

For the tortuosity (Table 2 and Figs. 10 and 11), the lengths of paths in HPC22 are considerably larger than the values in the other two films, for both τ_x and τ_y. For τ_y in HPC22, which is the tortuosity

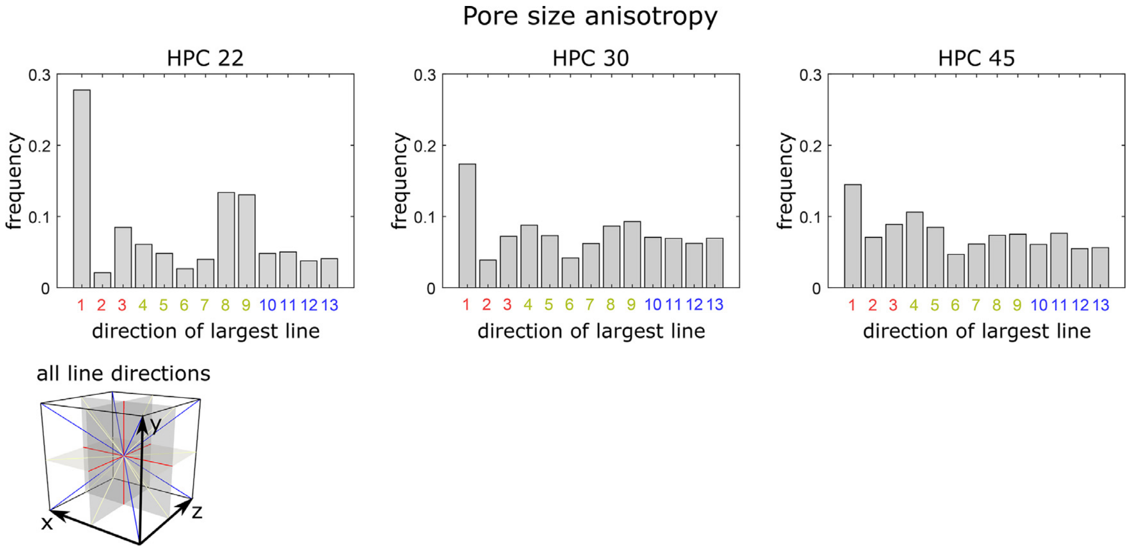

Fig. 6. The frequency of points in the pore space for which the line size in the chosen direction is larger than the line size in all other directions, shown for all three films. The line directions are numbered, showing the frequency for (1) the *x*-direction, (2) the *y*-direction and (3) the *z*-direction, the two diagonal directions in (4-5) the *xy*-plane, (6-7) the *yz*-plane and (8-9) the *xz*-plane, and (10-13) the four diagonal directions crossing the unit cube. The line directions are illustrated in the box in the lower left corner, and the three line colours (red, yellow/green, blue) are the same as in the numbering of the histogram-bars. (For interpretation of the references to color in this figure legend, the reader is referred to the web version of this article.)

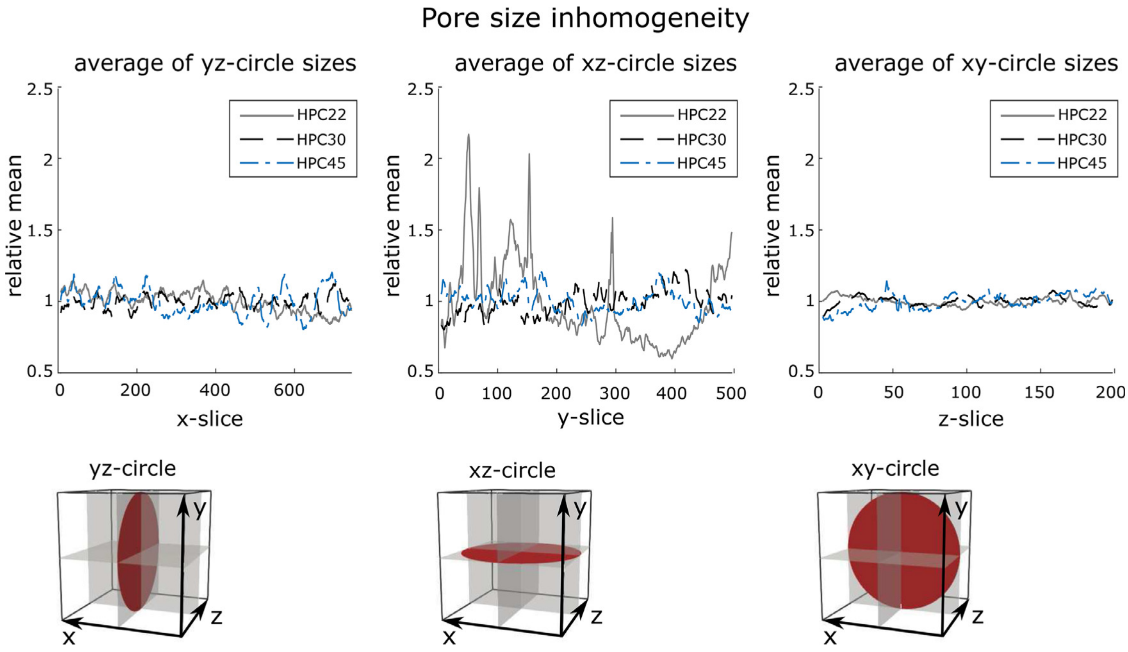

Fig. 7. The mean of (left) $ps_{circ,yz}$, (middle) $ps_{circ,xz}$ and (right) $ps_{circ,xy}$, computed for each slice in the direction perpendicular to the respective circle, i.e., the mean of the circle-pore size over each slice in (left) the *x*-direction, (middle) the *y*-direction and (right) the *z*-direction. Each curve was normalized by dividing by the mean of the respective circle-pore size computed over the full pore space. The circle orientations are illustrated in the boxes below the figures.

in the transport direction, the left half of the film is poorly connected with τ_y values above three (light blue areas). There is an area in the right half of the film which is better connected with τ_y around two (dark blue areas). The area with dark blue tortuosity in the yellow box corresponds to the part indicated by the yellow arrow on the right of HPC22 in Fig. 9.

The values of the tortuosities of τ_x in HPC22, and of both τ_x and τ_y in the other two films, are more homogeneously distributed throughout the films. The relative lengths of paths in the transport direction (τ_y) are about twice as large as the relative lengths of paths in the *x*-direction (τ_x) for HPC22. Paths in the transport direction are longer than paths in the *x*-direction for HPC30 as well, but the difference is smaller. For HPC45, the difference is quite small, except for the max-values. The pores in the layers with low porosities in Fig. 8 (marked with dashed frames), can be seen in Fig. 10 to have relatively high tortuosities in the *x*-direction. This trend is strongest in HPC22.

Connectivity measured by geodesic channel strength (path locations)

The main channels, i.e. parts of the pore structure with high geodesic channel strength, are of considerably higher strength in HPC22 compared to in HPC30. The yellow box in HPC22 in Fig. 12 contains a main channel with strength of 86%, i.e. 86% of all computed geodesic paths or around 8000 of the total 9000 computed geodesic paths, passed through this channel. In fact there are only two paths which connect the pore space above the yellow box with the pore space below; one on the left (main channel in gray with channel strength 14%) and the one mentioned above on the right (main channel in red with channel strength 86%). If these main channels were closed, the pore structure would no longer be connected, indicating that the area marked by the yellow box is a limiting layer that has a considerable effect on the connectivity of HPC22. The lowest tortuosities computed in the *y*-direction for HPC22 (Fig. 10, top left, dark blue pores), with values around two, correspond to geodesic paths that pass through the main channel on the right.

In contrast, the maximum geodesic channel strength in HPC30 and HPC45 are both under 11%, meaning that the paths are more well distributed across the whole pore space (Table 2) These differences in channel strengths between the films are also clearly visible in the histograms in Fig. 13.

Discussion

Pore shape: Since the ellipsoid-factor throughout was roughly equal to 2, the pores are relatively flat, and not spherical. The increasing elongation factors show that the shape of the pores nevertheless change with increasing porosity.

Table 2
Pore connectivity measures for the three films computed in the *y*-direction, showing the proportion of pores that are connected to the bottom and top, the MIP-pore size, the constrictivity, the tortuosity (also computed in the *x*-direction) and the channel strength. The median/mean, minimum, maximum and standard deviations are given for the MIP-pore size, the tortuosity, and the channel strength. The MIP-pore size values are given in μm.

	HPC22	HPC30	HPC45
Proportion connected pores, *y*-dir.	0.86	0.99	0.99
$ps_{\mathrm{MIP},y}$, median (min, max) [st. dev.]	0.05 (0.05, 0.75) [0.07]	0.35 (0.05, 1.15) [0.08]	0.50 (0.05, 2.35) [0.18]
Constrictivity, *y*-dir.	0.15	0.58	0.67
τ_x, median (min, max) [st. dev.]	1.27 (1.11, 2.17) [0.13]	1.10 (1.06, 1.43) [0.02]	1.08 (1.04, 1.38) [0.02]
τ_y, median (min, max) [st. dev.]	2.75 (2.07, 4.62) [0.49]	1.19 (1.10, 1.55) [0.04]	1.10 (1.04, 1.55) [0.02]
GeoChannels$_y$, median (min, max) [st. dev.]	0.012 (0.0001, 0.86) [0.060]	0.005 (0.0001, 0.11) [0.012]	0.004 (0.0001, 0.06) [0.006]

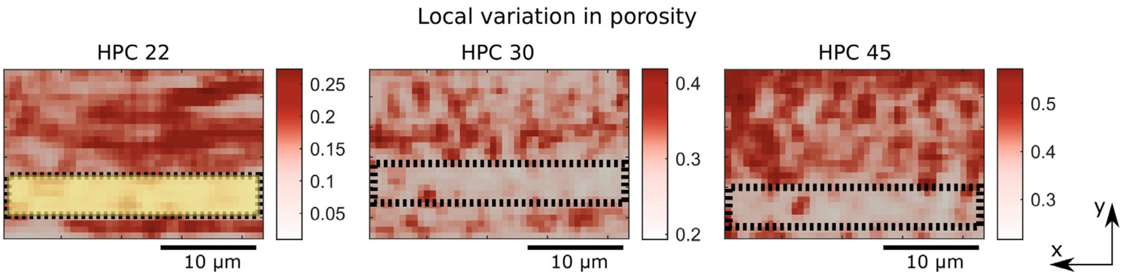

Fig. 8. Local porosity, computed for overlapping boxes resulting in values on a 43 × 28 × 1 grid. The dashed black frames indicate layers in the y-direction with low local porosity. The dashed frame is filled in with yellow with low opacity in HPC22, corresponding to the yellow boxes used for HPC22 in Figs. 9, 10 and 12. (For interpretation of the references to color in this figure legend, the reader is referred to the web version of this article.)

Inhomogeneity: The films were manufactured by depositing layers, one after the other, in the *xz*-plane. This may explain why the line size typically is shorter in the *y*-direction than in the *x*-direction, and why the variation in circle pore sizes $ps_{circ,xz}$ across slices is large in the *y*-direction for HPC22, but not in the other two circle pore size-directions. The sequential deposition of layers could also explain the high variation in local porosity in the *y*-direction in all three films, as well as the large difference found in connectivity, as measured by the tortuosity, in the *x*-direction compared to in the *y*-direction for both HPC22 and HPC30. This is interesting since the *y*-direction would be the direction of transport of drug through the films.

Percolation threshold: 22% pore volume fraction is close to the percolation onset for this material.[16] This means that above porosity 22% there is a sharp increase in how much HPC that is leached out, and thus a sharp increase in how large proportion of the HPC that is connected to the top and bottom of the unprocessed film. This may explain why the connectivity was much lower for HPC22 than for HPC30 and HPC45, as measured by the proportion of connected pores, the constrictivity, the geodesic tortuosity and the geodesic channels (Table 2 and Figs. 8-13). It may also explain why there is much larger variation in the circle pore size $ps_{circ,xz}$ across slices in the *y*-direction for HPC22 compared to in the other two films. See Fager et al.[44] for a detailed analysis of the diffusive transport properties of the three films, where it was concluded that the low connectivity in HPC22 considerably lowers the transport rate through the film.

Bias factors: The characterization results were influenced by boundary effects, effects of the binarization algorithm and effects of the sub-sampling done to obtain equal voxel distance in all dimensions. The influence of these bias factors are difficult to estimate. But since all three films have been treated in the same way, the characterization results should nevertheless be comparable between the three films. Even so, the different properties of the films may cause the bias to be different in different films. The

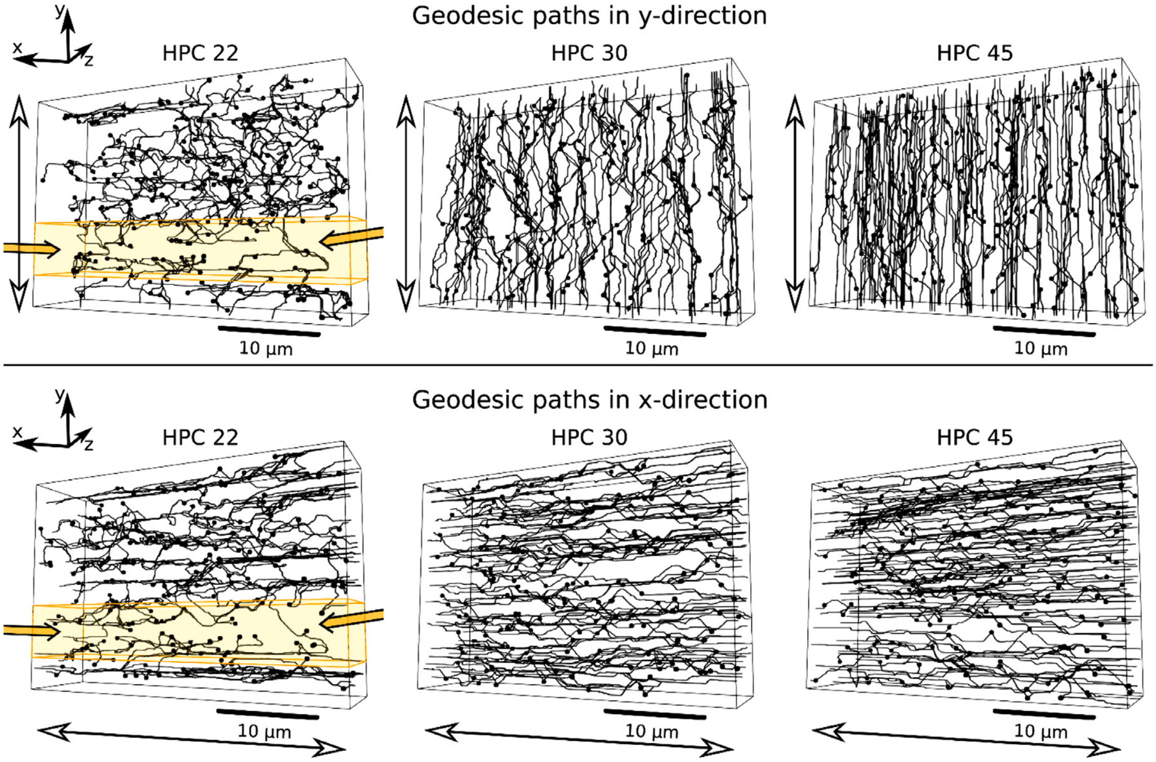

Fig. 9. 200 randomly chosen geodesic paths *GeoPath*(p) for HPC22 (left), HPC30 (middle) and HPC45 (right), computed in the *y*-direction (top row) and in the *x*-direction (bottom row). The point p is shown for each path as a black sphere and the directions the paths were computed in are indicated by double-headed arrows. A layer with poor connectivity in HPC22 is marked with a yellow box. The only two pathways through the yellow box taken by the geodesic paths are indicated by yellow arrows. (For interpretation of the references to color in this figure legend, the reader is referred to the web version of this article.)

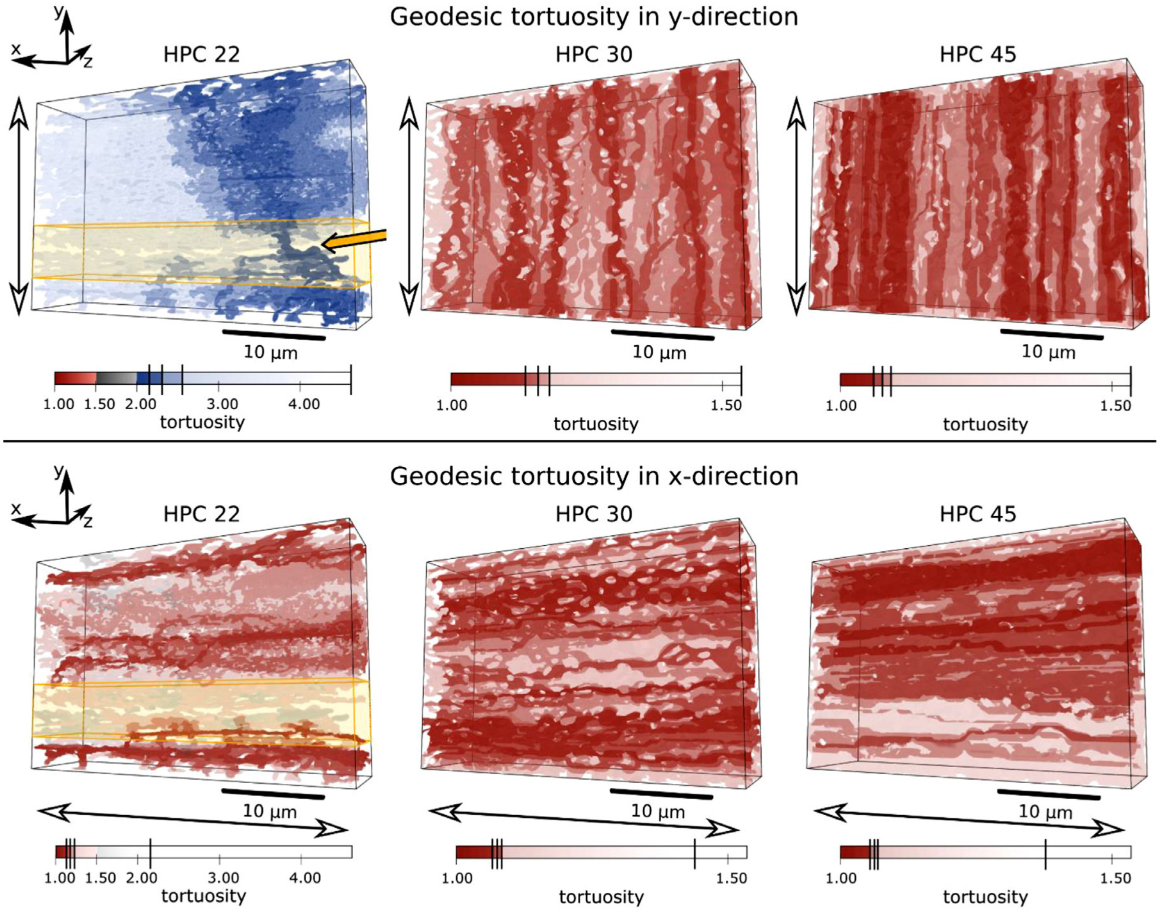

Fig. 10. Tortuosity for HPC22 (left), HPC30 (middle) and HPC45 (right), computed in the *y*-direction (top row) and in the *x*-direction (bottom row). The directions are indicated by double-headed arrows. A layer with poor connectivity in HPC22 is marked with a yellow box, and a yellow arrow corresponding to the yellow arrows on the right side of HPC22 in Fig. 9 is shown in the top left panel. The color scales: The same opaque color scale has been used for all six combinations of film/tortuosity direction. The difference in color lightness along the color scales is due to a layering of images of the tortuosity thresholded at the 10%, 25%, 50% and 100% quantile, with each image layer having a different opacity. See the supplementary material for more information about the image layering-method. The 10%, 25%, 50% and 100% quantiles are marked with vertical lines on the color bars. The color bar is shown cut off just above 1.5 for HPC30 and HPC45. (For interpretation of the references to color in this figure legend, the reader is referred to the web version of this article.)

proportion of connected pores should equal one if the whole film had been imaged, since the pores are leached out and therefore pores that are visible in the FIB-SEM images are pores that are connected to the boundaries of the film. That the proportion connected pores in HPC22 is much lower than in the other two films could be a combination of the bias factors and the low connectivity of the pores in HPC22. Similar effects could cause the tortuosity and channel results to be more biased for HPC22 as compared to the other two films.

New connectivity measure: The geodesic channel measure was found to provide interesting information about the pore structures, and in particular showed a big difference between HPC22 and the other two films. Even though both the tortuosity and channel measure are computed based on geodesic paths, the two characterization measures highlight different properties of the pore geometry (compare the top row of Fig. 10 with Fig. 12). The main geodesic channels for example show that paths through HPC22 are not just longer compared to the paths in the other

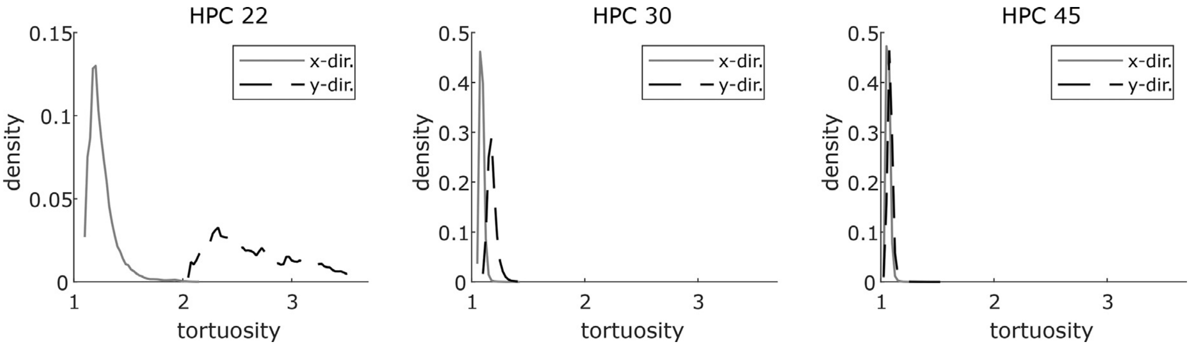

Fig. 11. Histograms of the data shown in Fig. 10.

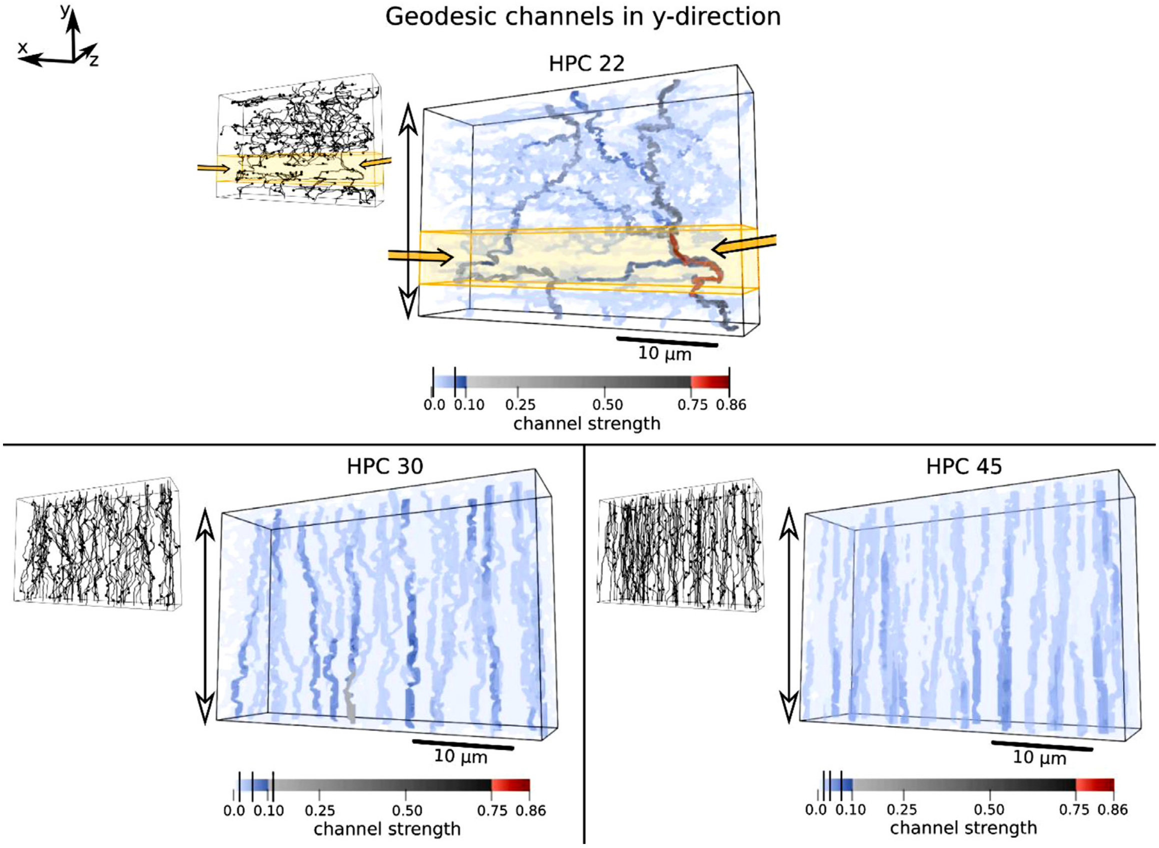

Fig. 12. Geodesic channel strength, computed in the *y*-direction (indicated by the double-headed arrows) from 9000 geodesic paths, shown for all three films. A layer with poor connectivity in HPC22 is marked with a yellow box and two main channels through the box are indicated by yellow arrows. The color scales: The same opaque color scale has been used for all three films. The difference in color lightness along the color scales is due to a layering of images of the channel strength thresholded at the 97%, 99.5% and 100% quantile, with each image layer having a different opacity. See the supplementary material for more information about the image layering-method. The 97%, 99.5% and 100% quantiles are marked with vertical lines on the color bars. The geodesic path illustrations from Fig. 9 are shown to the left of the corresponding geodesic channel strength. (For interpretation of the references to color in this figure legend, the reader is referred to the web version of this article.)

two films, as shown by the tortuosity, but behave in a radically different way. This is especially noticeable in the limiting layer (marked with a yellow box in Figs. 9, 10 and 12), through which there are two main channels that all 9000 computed geodesic paths pass through (indicated by yellow arrows in Fig. 12). As these are the only two pathways through the limiting layer, and the pore size is relatively small, we can conclude that there is a strong geodesic channel-bottleneck effect caused by the pore network structure in HPC22. This type of bottleneck is not captured by the existing constriction-bottleneck measures found in Berg,[14] Holzer et al.[15]; and Stenzel et al.[10]

New pore size measure: Taking maxima of pore sizes with respect to elongation and lines, and computing ellipsoid and elongation factors extracted interesting information about anisotropy in the three EC/HPC films.

Conclusions

In contrast to the common reporting of only porosity[7] and isotropic pore size measures, we have shown how the wider range of pore geometry characterization methods applied in this work can be used to identify interesting properties of the pore geometry of the EC/HPC

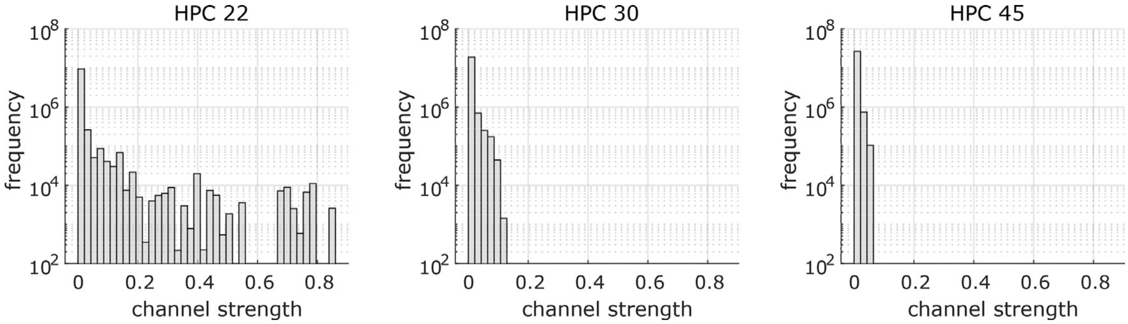

Fig. 13. Histograms of the data shown in Fig. 12.

films. Anisotropy results, showing a different behavior in the *y*-direction, i.e. in the direction of mass transport, which could be explained by the film-manufacturing process, were found. The HPC22 film was found to have considerably lower connectivity (Figs. 9-13, Table 2), to be less homogeneous and to have stronger anisotropy (Figs. 6-8, 10-13; Tables 1 and 2) compared to the other two films. This could be explained by the fact that HPC22 is close to the percolation threshold. The new geodesic channel measure also provided insights into the connectivity, complementing existing connectivity measures such as the geodesic tortuosity and constrictivity. The bottleneck effects caused by the pore network in HPC22, measured by the geodesic channel-strength, considerably lowers the diffusive transport rate in that film compared to in HPC30 and HPC45, see Fager et al.[44]

Author contributions

All authors participated in defining over-arching research goals, analysis of results and editing of the manuscript. S. Barman, advised by D. Bolin and H. Rootzén, invented and implemented the new characterization methods and drafted the manuscript. C. Fager, advised by E. Olsson, performed the microscopy imaging of the EC/HPC films and participated in drafting the manuscript. M. Röding performed the segmentation of the image data.

Supporting information available

Supporting information is available electronically. The .pdf-file contains information about the method used to compute the geodesic paths, as well as more detailed information about the method that was used to create the layered images. A comparison is made between layered images and the result obtained with standard 3-D volume renderings. There are also two videos which illustrate the connection between the layered images and successive thresholding of the 3-D results.

Conflicts of interest

There are no conflicts to declare.

Acknowledgments

We thank Aila Särkkä and everyone involved in the SSF project for valuable feedback. We also appreciate the feedback given at workshops organized by the Chalmers center SuMo Biomaterials and within the project COSIMA, both funded by Vinnova. Funding: This work was supported by the Swedish Foundation for Strategic Research [grant number AM13-0066], the Knut and Alice Wallenberg foundation [grant number 20012.0067], and the Swedish Research Council [grant number 2016-04187].

Supplementary materials

Supplementary material associated with this article can be found in the online version at doi:10.1016/j.xphs.2021.02.024.

References

1. Petersen E. Diffusion in a pore of varying cross section. *AIChE J*. 1958;5:343–345.
2. Siepmann J, Siegel R, Rathbone M, eds. *Fundamentals and Applications of Controlled Drug Delivery*. New York: Springer; 2012.
3. Torquato S. *Random Heterogeneous Materials: Microstructure and Macroscopic Properties. Interdisciplinary Applied Mathematics*. Springer; 2002.
4. Heng D, Tang P, Cairney J, et al. Focused-ion-beam milling: a novel approach to probing the interior of particles used for inhalation aerosols. *Pharm Res*. 2007;24 (9):1608–1617.
5. James J, Choi HW, Pharoah J. X-ray computed tomography reconstruction and analysis of polymer electrolyte membrane fuel cell porous transport layers. *Int J Hydrogen Energy*. 2012;37(23):18216–18230.
6. Anovitz L, Cole D. Characterization and analysis of porosity and pore structures. *Rev Mineral Geochem*. 2015;80(1):61–164.
7. Markl D, Strobel A, Schlossnikl R, et al. Characterization of pore structures of pharmaceutical tablets: a review. *Int J Pharm*. 2018;538:188–214.
8. Chiu S, Stoyan D, Kendall W, Mecke J. *Stochastic Geometry and its Applications*. 3rd ed. Chichester: John Wiley & Sons; 2013.
9. Peyrega C, Jeulin D. Estimation of tortuosity and reconstruction of geodesic paths in 3D. *Image Anal Stereol*. 2013;32(1):27–43.
10. Stenzel O, Pecho O, Holzer L, Neumann M, Schmidt V. Predicting effective conductivities based on geometric microstructure characteristics. *AIChE J*. 2016;62:1834–1843.
11. Barman S, Rootzén H, Bolin D. Prediction of diffusive transport through polymer films from characteristics of the pore geometry. *AIChE J*. 2019;65(1):446–457.
12. Van Brakel J, Heertjes PM. Analysis of diffusion in macroporous media in terms of a porosity, a tortuosity and a constrictivity factor. *Int J Heat Mass Transf*. 1974;9:1093–1103.
13. Dullien FA. *Porous Media: Fluid Transport and Pore Structure*. New York: Academic Press; 1979.
14. Berg C. Re-examining Archie's law: conductance description by tortuosity and constriction. *Phys Rev E Stat Nonlinear Soft Matter Phys*. 2012;86(4):0463.
15. Holzer L, Weidenmann D, Münch B, et al. The influence of constrictivity on the effective transport properties of porous layers in electrolysis and fuel cells. *J Mater Sci*. 2013;48(7):2934–2952.
16. Marucci M, Hjärtstam J, Ragnarsson G, Iselau F, Axelsson A. Coated formulations: new insights into the release mechanism and changes in the film properties with a novel release cell. *J Control Rel*. 2009;136(3):206–212.
17. Marucci M, Arnehed J, Jarke A, et al. Effect of the manufacturing conditions on the structure and permeability of polymer films intended for coating undergoing phase separation. *Eur J Pharm Biopharm*. 2013;83(2):301–306.
18. Andersson H, Hjärtstam J, Stadig M, von Corswant C, Larsson A. Effects of molecular weight on permeability and microstructure of mixed ethyl-hydroxypropyl-cellulose films. *Eur J Pharm Sci*. 2013;48(1):240–248.
19. Jansson A, Boissier C, Marucci M, et al. Novel method for visualizing water transport through phase-separated polymer films. *Microsc Microanal*. 2014;20(2):394–406.
20. Häbel H, Andersson H, Olsson A, Olsson E, Larsson A, Särkkä A. Characterization of pore structure of polymer blended films used for controlled drug release. *J Control Rel*. 2016;222:151–158.
21. Häbel H, Rajala T, Marucci M, et al. A three-dimensional anisotropic point process characterization for pharmaceutical coatings. *Spat Stat*. 2017;22:306–320.
22. Fager C, Barman S, Röding M, et al. 3D high spatial resolution visualisation and quantification of interconnectivity in polymer coatings. *Int J Pharm*. 2020;587 (119622).
23. Fager C, Röding M, Olsson A, et al. Optimization of FIB-SEM tomography and reconstruction for soft, porous, and poorly conducting materials. *Microsc Microanal*. 2020;26(4):837–845.
24. Gebäck T, Marucci M, Boissier C, Arnehed J, Heintz A. Investigation of the effect of the tortuous pore structure on water diffusion through a polymer film using lattice Boltzmann simulations. *J Phys Chem B*. 2015;119. 5520-5227.
25. Bassim N, Scott K, Giannuzzi LA. Recent advances in focused ion beam technology and applications. *Mrs Bull*. 2014;39(4):317–325.
26. Zschech E, Löffler M, Krüger P, et al. Laboratory computed X-ray tomography – a nondestructive technique for 3D microstructure analysis of materials. *Praktisc Metallogr*. 2018;55(8):539–555.
27. Vontobel P, Lehmann EH, Hassanein R, Frei G. Neutron tomography: method and applications. *Physica B*. 2016;385-386:475–480.
28. Röding M, Fager C, Olsson A, von Corswant C, Olsson E, Lorén N. Three-dimensional reconstruction of porous polymer films from FIB-SEM nanotomography data using random forests. *J Microsc*. 2020. https://doi.org/10.1111/jmi.12950.
29. MATLAB. *Version R2018a*. Natick, Massachusetts: The MathWorks Inc.; 2018.
30. LaValle S. *Planning Algorithms*. New York: Cambridge University Press; 2006.
31. Kallmann M, Kapadia M. *Geometric and Discrete Path Planning for Interactive Virtual Worlds. Synthesis Lectures on Visual Computing: Computer Graphics, Animation, Computational Photography, and Imaging*. Morgan & Claypool; 2016.
32. Cohen L, Kimmel R. Global minimum for active contour models: a minimal path approach. *Int J Comput Vis*. 1997;24(1):57–78.
33. Soille P. *Morphological Image Analysis: Principles and Applications*. 2nd ed. Berlin Heidelberg: Springer; 2004.
34. Lindquist W, Lee SM, Coker D, Jones K, Spanne P. Medial axis analysis of void structure in three-dimensional tomographic images of porous media. *J Geophys Res*. 1996;101(B4):8297–8310.
35. Hilfer R. Local porosity theory for flow in porous media. *Phys Rev B Conden Matter Mater Phys*. 1992;45(13):7115–7121.
36. Matheron G. *Eléments Pour Une Théorie Des Milieux Poreux*. Masson; 1967.
37. Camp J, Hann C, Johnson D, Tarara J, Robb R. Three-dimensional reconstruction of aqueous channels in human trabecular meshwork using light microscopy and confocal microscopy. *Scanning*. 1997;19(4):258–263.

38. Moore M. Quantitative analysis of interconnectivity of porous biodegradable scaffolds with micro-computed tomography. *J Biomed Mater Res A*. 2004;71(2):258–267.
39. Münch B, Holzer L. Contradicting geometrical concepts in pore size analysis attained with electron microscopy and mercury intrusion. *J Am Ceram Soc*. 2008;91(12):4059–4067.
40. Ayachit U. *The ParaView Guide: A Parallel Visualization Application*. Kitware; 2015. ISBN 978-1930934306.
41. Harrington B., Gould T., Hurst N., MenTaLgu Y. Inkscape. 2005.
42. VideoPad Professional. Version 7.39. NCH Software; 2019.
43. Barman S., Bolin D., Fager C., et al. MIST - a program package for visualization and characterization of 3D geometries. 2019.
44. Fager C., Hjärtstam J., Gebäck T., et al. Unpublished results. Correlating 3D porous structure with mass transport properties in polymer films using FIB-SEM tomography.